Karbala International Journal of Modern Science

Manuscript 3366

Synthesis of ZnO: ZrO2 Nanocomposites Using Green Method for Medical Applications

Mohammed J. Tuama

Maysoon F. Alias

Synthesis of ZnO: ZrO2 Nanocomposites Using Green Method for Medical Applications

Abstract

These days, nanocomposites are very popular, especially in medical applications. The spread of diseases in general, and those caused by microbes and cancerous diseases in particular, and the increased resistance of these diseases to antibiotics, have led to the need for the rapid, low-cost, and environmentally friendly production of nanocomposites. To create the chemical G-ZnO: ZrO2 and S-ZnO: ZrO2 (green technique), two different plant extracts were utilized: Z. officinal and S. aromaticum. The effective synthesis and acceptable properties features of the nanoparticles were confirmed using characterization techniques such as X-ray diffraction (XRD), Fourier transform infrared (FTIR) , diffuse reflectance spectroscopy (DRS), Field emission scanning electron microscopy (FESEM), energy-dispersive X-ray spectroscopy (EDX) and zeta potential. It turned out that the prepared materials (G-ZnO: ZrO2 and S-ZnO: ZrO2) were nanocomposites and polycrystalline structure with nano crystallite sizes. There was also a new peak that appeared at $2\theta = 29.4$ for G-ZnO: ZrO2 as a compound. FTIR was performed to investigate the nature of functional groups in the active compounds responsible for the formation of nanoparticles. There was a direct energy gap with values of 3.15 eV and 3.25 eV for the G-ZnO and S- ZnO samples, respectively, and 4.6 eV and 4.7 eV for the G-ZrO2 and S- ZrO2 samples, respectively. The morphological examination reveals some spherical nanoparticles randomly dispersed over the needle-like particles for G-ZnO: ZrO2 with 33nm average particle size, while S-ZnO: ZrO2 contains spherical, lobed nanoparticles with generally smooth agglomerates with 37nm average particle size. The prepared materials were tested on microbes using agar diffusion method. The results indicate slight superiority over the sample G-ZnO: ZrO2, however the sample S-ZnO: ZrO2 succeeded in killing microbes. As for anticancer activity of G-ZnO: ZrO2 and S-ZnO: ZrO2 nanocomposites for colon cancer cell lines (HCT-116 and LoVo), it was found that the manufactured substance helped destroy the cell, cause apoptosis, and show high levels of killing. This paper contributes to the field by presenting a viable approach to treat antibiotic resistance through nanotechnology.

Keywords

Green synthesis; Nanocomposites zinc oxide and zirconium oxide; Zingiber officinale; Syzygium aromaticum; Antimicrobial; Anticancer activity application

RESEARCH PAPER

Synthesis of ZnO: ZrO_2 Nanocomposites Using Green Method for Medical Applications

Mohammed J. Tuama, Maysoon F. Alias*

Physics Department, College of Science, University of Baghdad, Jadriya, Baghdad, Iraq

Abstract

These days, nanocomposites are very popular, especially in medical applications. The spread of diseases in general, and those caused by microbes and cancerous diseases in particular, and the increased resistance of these diseases to antibiotics, have led to the need for the rapid, low-cost, and environmentally friendly production of nanocomposites. To create the chemical G-ZnO: ZrO_2 and S−ZnO: ZrO_2 (green technique), two different plant extracts were utilized: *Z. officinal and S. aromaticum*. The effective synthesis and acceptable properties features of the nanoparticles were confirmed using characterization techniques such as X-ray diffraction (XRD), Fourier transform infrared (FTIR), diffuse reflectance spectroscopy (DRS), Field emission scanning electron microscopy (FESEM), energy-dispersive X-ray spectroscopy (EDX) and zeta potential. It turned out that the prepared materials (G-ZnO: ZrO_2 and S−ZnO: ZrO_2) were nanocomposites and polycrystalline structure with nano crystallite sizes. There was also a new peak that appeared at $2\theta = 29.4$ for G-ZnO: ZrO_2 as a compound. FTIR was performed to investigate the nature of functional groups in the active compounds responsible for the formation of nanoparticles. There was a direct energy gap with values of 3.15 eV and 3.25 eV for the G-ZnO and S− ZnO samples, respectively, and 4.6 eV and 4.7 eV for the G-ZrO_2 and S− ZrO_2 samples, respectively. The morphological examination reveals some spherical nanoparticles randomly dispersed over the needle-like particles for G-ZnO: ZrO_2 with 33 nm average particle size, while S−ZnO: ZrO_2 contains spherical, lobed nanoparticles with generally smooth agglomerates with 37 nm average particle size. The prepared materials were tested on microbes using agar diffusion method. The results indicate slight superiority over the sample G-ZnO: ZrO_2, however the sample S−ZnO: ZrO_2 succeeded in killing microbes. As for anticancer activity of G-ZnO: ZrO_2 and S−ZnO: ZrO_2 nanocomposites for colon cancer cell lines (HCT-116 and LoVo), it was found that the manufactured substance helped destroy the cell, cause apoptosis, and show high levels of killing. This paper contributes to the field by presenting a viable approach to treat antibiotic resistance through nanotechnology.

Keywords: Green synthesis, Nanocomposites zinc oxide and zirconium oxide, Zingiber officinale, Syzygium aromaticum, Antimicrobial, Anticancer activity application

1. Introduction

The manuscript provides an investigation into the production of ZnO: ZrO_2 nanocomposites through an eco-friendly approach, particularly highlighting their relevance in medical settings. Nanocomposites and nanoparticles produced by the green synthesis method are free of toxic pollutants, which makes them ideal for biological and medical applications because they have unique chemical and physical properties [1]. This method is important because of its low environmental impact, and the samples produced in this way can be taken into consideration in practical applications, especially in drug delivery, antimicrobial coatings, or biosensors [2]. Green synthesis has a bottom-up approach to building nanoparticles, atom by atom and molecule by molecule, to form molecules. Their small size and biosynthesis methods characterize the largest molecules produced. This feature allows the formation of a large number of nanoparticles in a short time. The obtained nanoparticles have few defects, and they are characterized by a homogeneous composition [1,3].

Received 9 May 2024; revised 25 July 2024; accepted 29 July 2024.
Available online 17 September 2024

* Corresponding author.
E-mail address: may20131313@yahoo.com (M.F. Alias).

https://doi.org/10.33640/2405-609X.3366

The use of plant extracts in the manufacture of composite has the advantage of being more stable, easily accessible and safe to use. Plant extracts are essential because they contain compounds that contribute to the production of nanocomposites, which function as stabilizing and capping agents. Plants have more benefits than biological systems in forming compounds such as algae or fungi [4]. To enhance substances properties for various applications, one can synthesize two or more materials as compounds [5]. Nanocomposites are manufactured with the goal of facilitating a significant flexibility and enhancing the essential physical characteristics of substances. This aim is realized through the utilization of nanoscale building units, encompassing multiple elements, each possessing distinct and significant attributes [6]. Nanocomposites exhibit unique characteristics that are appropriate for applications in the biomedical field and packaging [7]. Zirconium dioxide (ZrO_2) is a mineral oxide that can be used in medical applications because it is not hazardous and has the benefits of being cost effective, environmentally friendly, and versatile in its uses. Additionally, it has a large band gap ranging from 5.0 to 5.5 eV [8,9]. Being mechanically more robust and more biocompatible than other conventional ceramic materials, it is a highly advanced biomaterial used in the medical sector [10]. Much research has shown that ZrO_2 crystals can contain phase structures: monoclinic (m), tetragonal (t), and cubic (c), i.e. three different types [11]. Zinc oxide has the chemical formula ZnO, which is an inorganic semiconductor [12]. Slightly yellowish-white powder, insoluble in water. There are three phases of the structures: the first is hexagonal (wurtzite), the second is cubic (zinc alloy), and the last is cubic (rock salt or Rochelle salt) [13,14]. It is one of the most interesting metal oxides for several reasons: the first is 3.37 eV energy gap, low -toxicity and the last is its physical and chemical stability [12]. The compound ($ZnO-ZrO_2$) has been produced by the green synthesis method using rubber (Ficus elastic) for biological applications [15]. The research area revolves around the production of nanocomposites using green synthesis with *Z. officinal* and *S. aromaticum* and tested for medical applications.

2. Experimental work

2.1. Materials

Both the flower buds of *S. aromaticum* and the ground roots of *Z. officinale* are available and can be purchased from local markets; they are carefully washed with distilled water (DW) to remove impurities. Ammonium hydroxide (NH_4OH), zirconyl nitrate $ZrO(NO_3)_2.H_2O$ and (EX-Pure) hexahydrate zinc nitrate $Zn(NO_3)_2.6H_2O$ (96.0–103.0 % pure) were purchased from Indian companies Alpha Chemika, Oxford, and Central Drug House (CDH), respectively.

2.2. Experimental part

The roots of *Z. officinale* and flower buds of *S. aromaticum* were grind using an electric grinder after dried from moisture and then their powder was stored in plastic containers. The plant powder was weighed 1 g, then 10 ml DW was added to it (1:10), and at 70 °C, it was stirred for 30 min. In order to filter the planktonic extracts, I use Whatman No. 1, at a temperature of 4 °C, plant extract sample containers [16,17]. Each extract was prepared individually, as shown in Fig. 1.

2.3. Composition ZnO: ZrO_2 NPs

Composition ZnO: ZrO_2 NPs were produced utilizing a green method by adding zinc nitrate

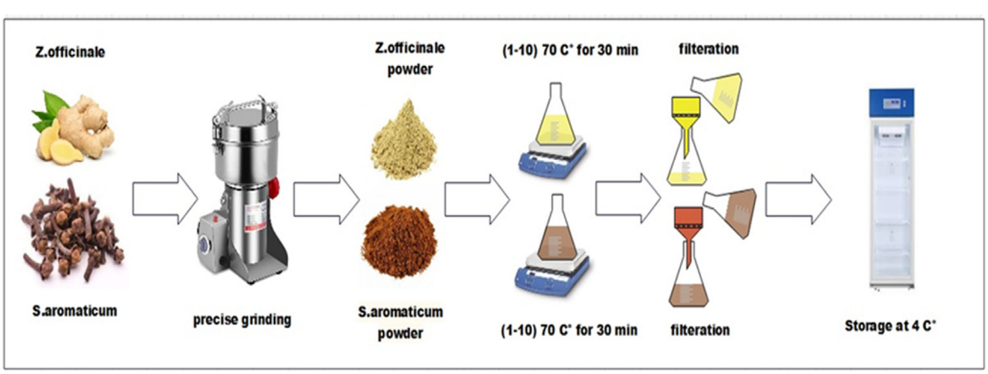

Fig. 1. Steps to make aqueous extracts from flower buds of S. aromaticum *and the ground root of* Z. Officinale.

hexahydrate and zirconyl nitrate in a ratio of 1:1−100 ml DW to reach a concentration of 1 M using Equation (1) [18]:

$$M_o = \frac{W_t}{M.W_t} * \frac{1000}{v} \quad (1)$$

where M_o is molar concentration (mol/l), M. W_t is material molecular weight (g/mol),V is solution volume (ml) and W_t is weight (g).

Next, the plant extract was added in an amount of 25 ml, the beaker was placed over the magnetic stirrer, and each sample was prepared in a time of 1 h and a temperature of 70−80 °C. During preparation, NH_4OH was added with a purity of 98% [15]. The next stage is a centrifuge at 4000 rpm for 15 min. The final product was rinsed with (DW) until it reached a pH of 7 [19]. Next, the resulting mixture was placed in a crucible at 500 °C for 2 h, i.e., heated [20,21] (see Fig. 2).

2.4. Antimicrobial tests for nanocomposites

The nanocomposites manufactured by the green synthesis method G-ZnO:ZrO_2 and S−ZnO:ZrO_2 were tested against (*S. Aureus*) *Staphylococcus aureus*, (*E. Coli*) *Escherichia coli*, (*B. Subtilis*) *Bacillus subtilis*, and (*C. Albicans*) *Candida Albicans*. These were done in addition to the agar diffusion method. Mueller-Hinton agar was used to evaluate the microbial susceptibility of ZnO: ZrO_2 nanocomposites. Mueller-Hinton agar was prepared according to the manufacturer's directions and poured into Petri dishes to reach a mean thickness of approximately 1.0 cm, autoclaved for 15 min at 121 °C, and then allowed to solidify. The overnight turbidity of (*S. Aureus, E. Coli, B. Subtilis, and C. Albicans*) is 10^8 CFU/ml using the standard Mackfer ground technique. A cotton swab was soaked in each microbial growth under investigation, wiped on the surface of Mueller-Hinton agar, and left for 30 min at 25 °C. Using a needle, 6 mm holes were made in the agar. The holes were then filled with 100 μl of nanocomposites G-ZnO: ZrO_2 and S−ZnO: ZrO_2 at a 100 μg/ml concentration. All dishes were incubated for a period of time of 24−72 h, at a temperature of 37 °C, and the zones of inhibition were determined in (mm) for each sample to find which materials had the best antimicrobial activity [19,22,23].

2.5. Anticancer tests for nanocomposites

Anticancer activity of G-ZnO: ZrO_2 and S−ZnO: ZrO_2 nanocomposites for colon cancer cell lines (HCT-116 and LoVo) on live cancer cells. When cells were seeded at a density of 5000 cells per well on 96-well plates and incubated for 24 h before experiments, cells were washed to pH 7.4 (PBS) and incubated in a fresh medium containing different concentrations of samples, i.e., both G-ZnO: ZrO_2 and S−ZnO: ZrO_2 (1000, 500, 250, 125, and 62.5 μg/ml), for 72 h. A colorimetric assay called MTT was conducted to assess the cytotoxic impact of the materials at various doses. Following a 72 h incubation period at 37 °C in a humidified atmosphere with 5% CO_2, MTT (0.5 mg/ml in PBS) was introduced into each well. The plate was then incubated for a further 4 h at 37 °C. The produced formazan was dissolved in 100 μl of DMSO by gently shaking it at 37 °C. Subsequently, an ELISA reader was employed to quantify the spectroscopic absorption of the blue-purple formazan dye at a wavelength of 570 nm [24]. Equation (2) is used to calculate the relative cell viability of colon cancer.

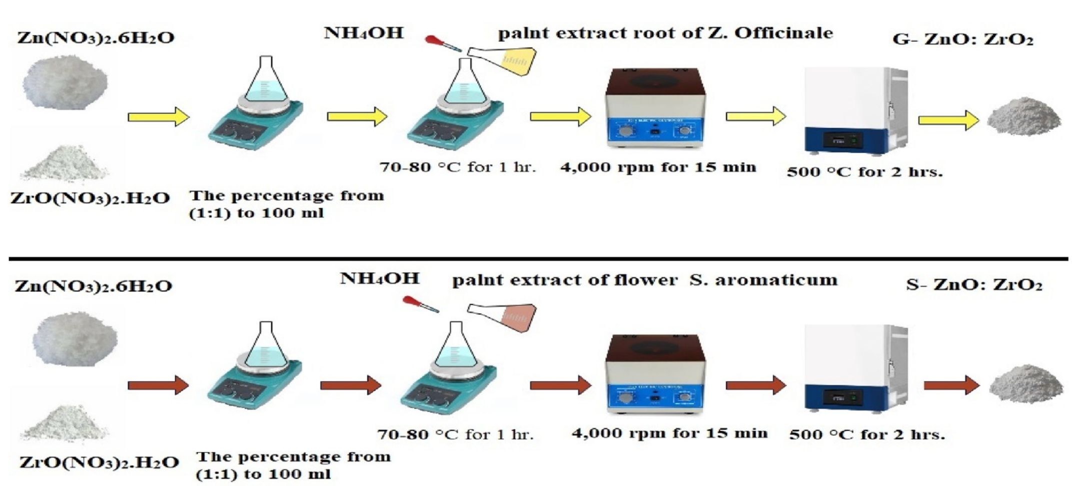

Fig. 2. Green synthesis steps to produce ZnO:ZrO_2 NPs formulations.

$$\text{Relative Cell viability} = \frac{\text{Average O.D. value for test}}{\text{Average O.D. value for control}} \times 100\% \quad (2)$$

2.6. Characterization methods

The composite green ZnO:ZrO_2 nanocomposites were analyzed by XRD device, model: PW1730, which is a device made in the United States of America by Philips. To calculate the average crystallite size and the crystal structure of nanocomposites, the functional group analysis was studied using a Fourier transform infrared spectrophotometer in the 400-4000 cm^{-1} frequency range.

Analysis of solid-phase ZnO:ZrO_2 nanocomposites The analysis included using a KBr pellet. The samples were scanned thrice, the sampling rate was taken, and the difference between one scan and another was (±5). Furthermore, the aim is to identify organic and inorganic biomolecule residues in nanocomposites (ZnO:ZrO_2), A Dutch-made Avantes Avaspec-2048 spectrophotometer was used to measure the wavelength band gap, Using a Tescan Mira 3 15 kV field emission scanning electron microscope (FESEM), Width is the identifier of the morphology of the sample, as well as calculating the particle size through this examination. Samples were studied using a 15 kV Tescan Mira 3 with an energy-dispersive X-ray (EDX) machine from the Czech Republic. The examination aims to indicate the absence of impurities and the purity of the ZnO:ZrO_2 nanocomposite, and Zeta potential measurements were performed using a Horiba Scientific Nano Particle SZ-100 laboratory instrument. It is possible to know the values of surface charges of nanocomposite.

3. Results and discussion

The X-ray diffraction (XRD) was investigated for G-ZnO: ZrO_2 and S–ZnO: ZrO_2 samples powder. The G-ZnO: ZrO_2 sample can be shown as ZrO_2 polycrystalline with two phases (tetragonal and monoclinic) structures, and ZnO has one stage and is crystallized with a hexagonal wurtzite structure. Fig. 3 gives the structural and geometric parameters. The XRD pattern of G-ZnO: ZrO_2, with a tetragonal crystal structure of ZrO_2, exhibits peaks at $2\theta = 30.26°$ and $50.28°$, which corresponds to the (101) and (112), respectively. These peaks agree with the data provided by the JCPDS card: (96-152-5707). The XRD pattern for G-ZnO: ZrO_2, ZrO_2 structural monoclinic has peaks at $2\theta = 24.09°$, $28.24°$, $45.5°$ and $35.33°$corresponding to (011), (11-1), (212) and (200) planes, respectively, matching the data of JCPDS card: (96-152-2144),whereas ZnO structural hexagonal wurtzite has peaks at two theta equal to 31.76°,34.45°,36.25°,47.55°,56.58°,62.89°,67.95°,69.07° and 76.96°, corresponding to (100), (002), (101), (012), (110), (013), (112), (201), and (202) planes, matched by the data of JCPDS card: (96-900-4180). It is also noted that the peak located at $2\theta = 29.4$ is a new phase that may indicate the formation of a new material as compound. The reason for the appearance of the peak located at this 2θ may be due to the change in positions of zirconium instead of zinc, as the ionic radius of zirconium is (0.72) A° [25] and the ionic radius of zinc is (0.74) A° [26]. This may allow sites to be exchanged, or there may be a role for plant-associated organic bonds to contribute to shifting the positions of both zinc and zirconium in this peak. The XRD pattern for S–ZnO: ZrO_2, ZrO_2 structural tetragonal has peaks at $2\theta = 30.25°$, $35.3°$, $50.38°$, $59.41°$, $60.44°$ and $74.65°$ corresponding to (011), (110), (112), (013), (121), and (220) planes,

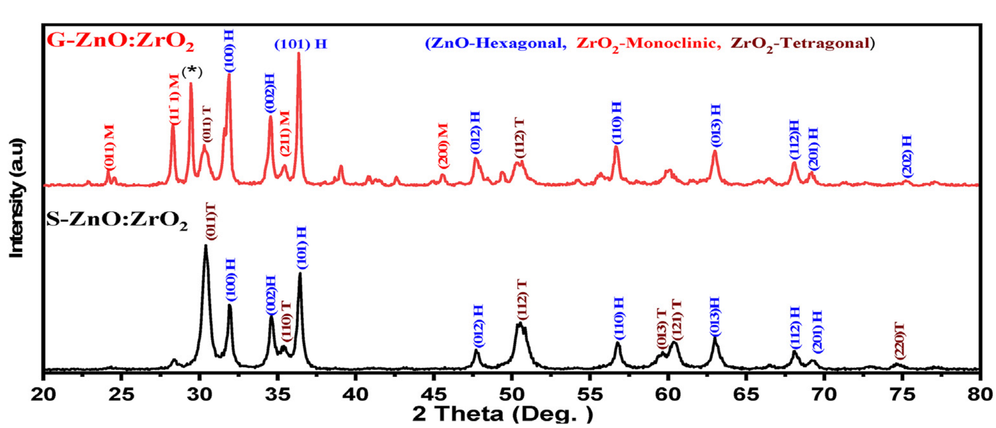

Fig. 3. XRD spectra of nanocomposites (a) G-ZnO: ZrO_2 and (b) S–ZnO: ZrO_2.

respectively, which match the data of JCPDS card: (96-230-0613) and ZnO structural hexagonal wurtzite has peaks at $2\theta = 31.8^\circ, 34.47^\circ, 36.28^\circ, 47.6^\circ, 56.63^\circ, 62.95^\circ, 68.03^\circ$, and 69.16°, corresponding to (100), (002), (101), (012), (110), (013), (112), and (201) planes, respectively, matched by the data of JCPDS card: (96-900-4181). The Scherrer formula Equation (3) [27] can be used to find the average crystallite size for each sample. For the composite G-ZnO: ZrO_2 and S−ZnO: ZrO_2 NPs, the average crystallite sizes were 24.48 nm and 21.84 nm, respectively. The acquired XRD results for composite ZnO: ZrO_2 agree with those published in prior studies [21,28].

$$D = k\,\lambda / \beta \cos\theta \tag{3}$$

where the crystallite size of the crystal is D, the Scherrer's constant (k) is (0.9), X-ray wavelength (0.15406 nm) is λ, the width of the XRD peak at half height is β, and the Bragg diffraction angle is (θ) [27]. The W−H and SSP plots explain the analysis of XRD data using Williamson-Hall (W−H) and size-strain plot (SSP) methods. These techniques are used to determine crystallite size and lattice strain by analyzing the broadening of diffraction peaks. It is possible to use Equation (4) for W−H, while for SSP use Equation (5) [29].

$$\beta \cos\theta = \frac{k\lambda}{D} + 4\varepsilon \sin\theta \tag{4}$$

where ε is the micro-strain.

$$(\beta \cos\theta)^2 = \left(\frac{k\lambda}{D}\right)^2 + (4\varepsilon \sin\theta)^2 \tag{5}$$

$(\beta \cos(\theta))^2$ is plotted on the y-axis, whereas $(\sin(\theta))^2$ is plotted on the x-axis. The intercept and slope of this plot provide information about the crystallite size and the micro-strain respectively.

From Fig. 4, one can observe the W−H and SSP for G-ZnO:ZrO_2 and S− ZnO:ZrO_2 samples, from which the average crystallite sizes for each sample can be calculated as shown in Table 1. Scherrer equation, Williamson-Hall model, and strain-volume plot method are used to determine the structure properties. The crystallite size determined using the W−H diagram was always larger than that obtained from the Scherrer formula for all sample compositions. This can be seen in Table 1. Scherrer's formula assumes a uniform pressure distribution

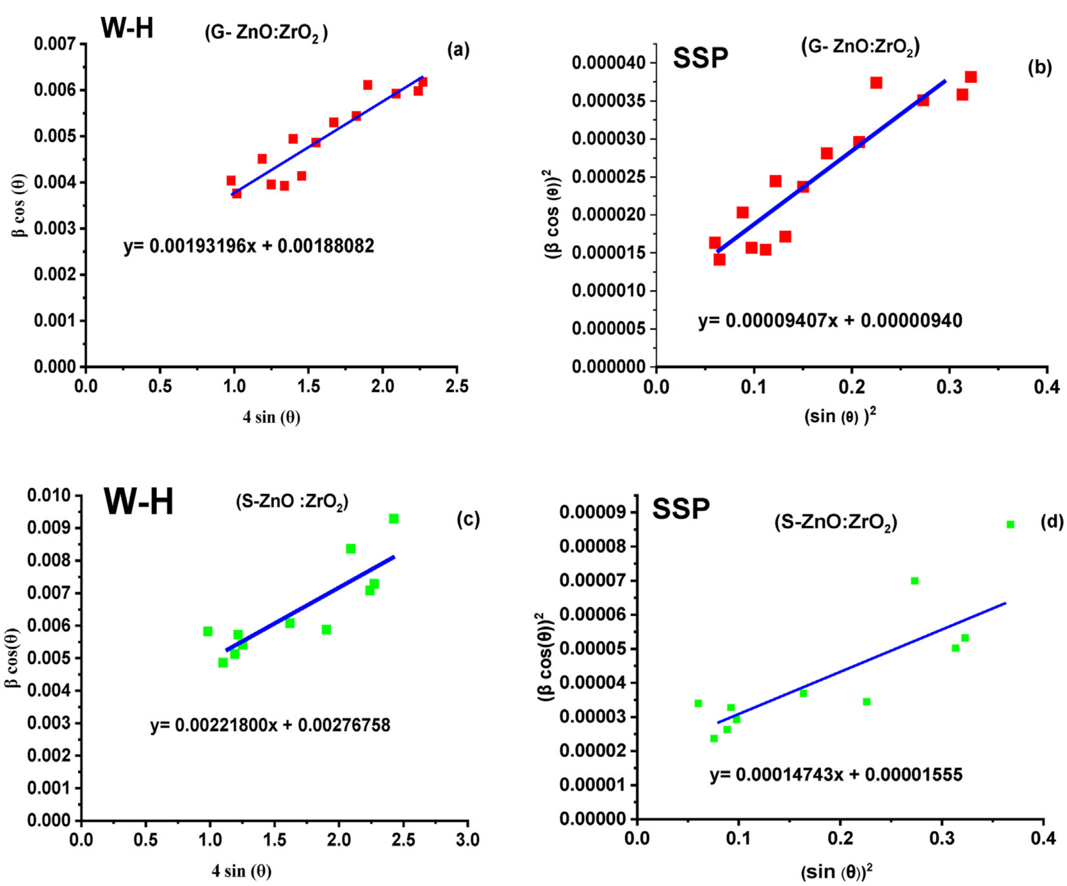

Fig. 4. The W−H and SSP of G-ZnO:ZrO_2 and S−ZnO:ZrO_2 samples.

Table 1. The crystallite sizes and micro-strain values for G-ZnO:ZrO$_2$ and S–ZnO:ZrO$_2$using three method.

Method	G-ZnO:ZrO$_2$		S–ZnO:ZrO$_2$	
	Crystallite size (nm)	Micro-strain	Crystallite size (nm)	Micro-strain
Scherrer	24.48		21.84	
W–H	73.71	0.00193	45.55	0.002218
SSP	50.09	0.00485	35.16	0.006071

within the crystals, which may not be the case in reality. In contrast, the W–H plot takes into account the sum of the effects of both strain and crystallite size, providing a more comprehensive analysis of crystallite size and strain distribution. This additional consideration can lead to larger crystal sizes in the W–H diagram. As for SSP, it depends on the sum of the square of strain and crystallite size, its value may be less than W–H for the same sample.

FTIR equipment, the aim is to identify the remnants of organic and inorganic biomolecules in the (ZnO: ZrO$_2$) compound Fig. 5 depicts the IR spectra of the G-ZnO: ZrO$_2$ and S–ZnO: ZrO$_2$ samples calcined at 500 °C for 2 h, also the plant extract (*Z. officinale root*) and extract (*S. aromaticum* flower). The main functional groups of *Z. officinale* root extract can be observed in Fig. 5, while the observed peaks are (3445, 2983, 1585, 1445, 923, 648, and 577) cm^{-1} represent (OH) [28], carboxylic acid (RCOOH) [29], (C–H) [30], aromatic (C=C) [28,31], terpenes like zingiberene C=C [30], phenol (O–H) [28] and (C–Br) [32], respectively. In the FTIR spectra of G-ZnO: ZrO$_2$, the presence of organic compounds has led to broadband coupling at 3454 cm^{-1} utilizing expansion vibrations in the broad range (OH) as presented in Fig. 5; the peaks detected are 2977, 1576, 1419, 1012, and 923 cm^{-1}. The peak at 1576 cm^{-1} has a significant effect due to aromatic components. Those at 619 cm^{-1}, qualified for stretching bond of the Zn–O, confirm the formation of the nanocomposite G-ZnO: ZrO$_2$ components present on the surface of the nanocomposite [33], wherein the region, the peak at 1012 cm^{-1} generally indicates that Zr–O binding domains were present. It was typical of zirconia [34]. One can see from Fig. 5, the main functional groups of *S. aromaticum* flower extract can be observed, while the observed peaks are 3451, 2970, 2353, 1585, 1386, 1230, 1067, 924 and 765 cm^{-1}, represent (O–H) stretching vibrations [34,35], alkyl CH stretch (sp^3) [36], (C–O) [35], aromatic (C=C) [30], (CH$_3$) methyl [35], (CH$_3$) methyl [35], (C–H) amino acid [37], (C–H) limonene [37], and (CH$_2$) eugenol groups [37], respectively. From the FTIR spectra of nanocomposite S–ZnO: ZrO$_2$, one can deduce the presence of organic compounds, including different polyphenols, carboxylic, aromatic acids, terpenes, and phenols. It has led to broadband coupling at 3434 cm^{-1} utilizing expansion vibrations in the broad range (OH) as presented in Fig. 5; the peaks observed are (2974, 1575, 1415, 1012, and 649) cm^{-1}. The 1575 cm^{-1} peak has a significant effect due to aromatic components. The peak at 649 cm^{-1}, qualified for stretching bond of (Zn–O), confirms the formation of nanocomposite S–ZnO:ZrO$_2$ [33]. It is attributed to the extension of the (Zr–O) bond and confirmation of the formation of nanocomposite S– ZnO: ZrO$_2$. A high peak of 1012 cm^{-1} can be observed. It generally indicates that Zr–O binding domains were present. It was typical of zirconia [34]. The positions of the peaks were changed somewhat in Fig. 5. The impact of the plant extract in each sample and the variation in the 500 °C calcination temperature due to both effects are two possible explanations for the small

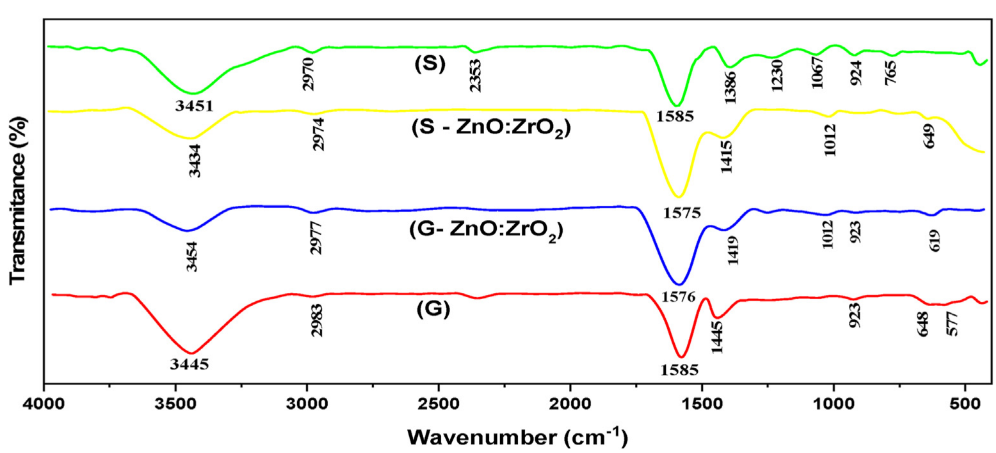

Fig. 5. FTIR spectra of (G) aqueous plant extract of Z. officinale, *(S) aqueous plant extract of* S. aromaticum, *(G-ZnO: ZrO$_2$) nanocomposite, which is produced by plant extract of* Z. officinale, *and (S–ZnO: ZrO$_2$) nanocomposite, which is produced by plant extract of* S. aromaticum.

change. It can be seen that the S–ZnO–ZrO_2 sample has its peak at 2434 cm^{-1}, while the G-ZnO-ZrO_2 sample may have a peak at 2344 cm^{-1}. Residues of phytochemicals and how they affect the material may cause subtle changes. The temperature at which powder phase samples are calculated removes the majority of chemical bonds.

Using diffuse reflectance spectroscopy (DRS), the optical properties are studied for G-ZnO: ZrO_2 and S–ZnO: ZrO_2 nanocomposites sample powders produced by the green synthesis method. A wavelength function of the sample's reflectance spectra in the 200–1000 nm spectral area was examined. Figs. 6 and 7 display the UV and visible (DRS) of the nanocomposites G- ZnO: ZrO_2 and S– ZnO: ZrO_2 samples. One can notice that they have a direct energy gap with values of 3.15 eV and 3.25 eV for the G-ZnO and S– ZnO samples, respectively. These results go in line with other researchers [38], whereas 4.6 eV and 4.7 eV for the G-ZrO_2 and S–ZrO_2 samples, respectively.The present results agree with Kianfar et al. [39]. Energy gaps can also interfere with each other, which leads to the overlap of levels and the appearance of a standard energy gap in the sample G-ZnO: ZrO_2. The direct energy gap appears at 3.92 eV. This interference is likely due to the formation of new compound material that agrees with XRD results where a new peak is found.

FESEM studies the morphological characteristics of the nanocomposite particles prepared by green synthesis using plant extracts *Z. officinale* and *S. aromaticum* to obtain the samples (G-ZnO:ZrO_2, and S–ZnO:ZrO_2), respectively. Fig. 8, reveals some spherical nanoparticles randomly dispersed over the needle-like particles for G-ZnO:ZrO_2. The particle size ranges were from 10 to 90 with an average of 33 nm [40]. The S–ZnO:ZrO_2 in Fig. 9, contains spherical, lobed nanoparticles with generally smooth agglomerates. The particle size ranges were from 5 to 90 with an average of 37 nm [41]. This difference in shape may be due to the extract used in preparing the substance, noting that the EDX examination of each sample proves the presence of zinc, which is present between 10 and 1 keV [42]. As for zirconium, it can be observed in places from 0.5 to 2.5 keV [43]. The absence of impurities indicates the purity of the material.

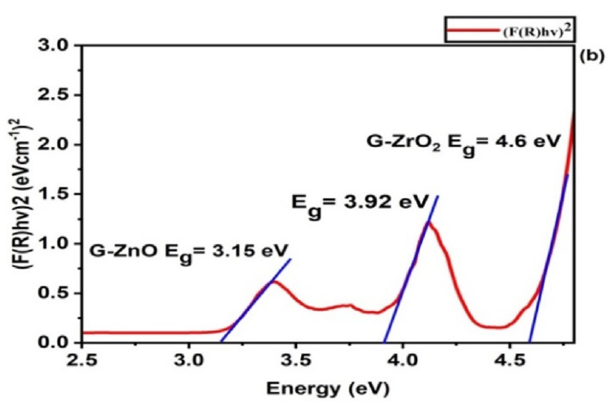

Fig. 6. (F(R) hv) ^{2} vs. energy of G-ZnO: ZrO_2.

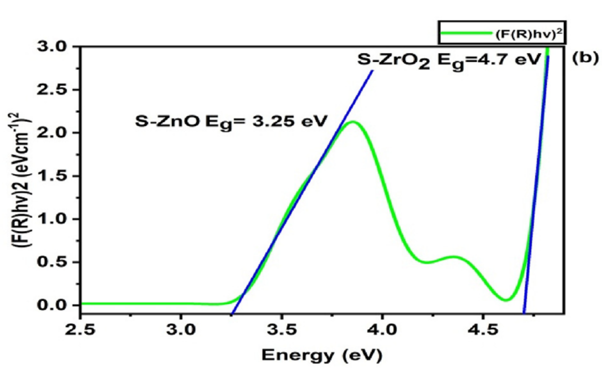

Fig. 7. (F(R) hv) ^{2} vs. energy of S– ZnO: ZrO_2.

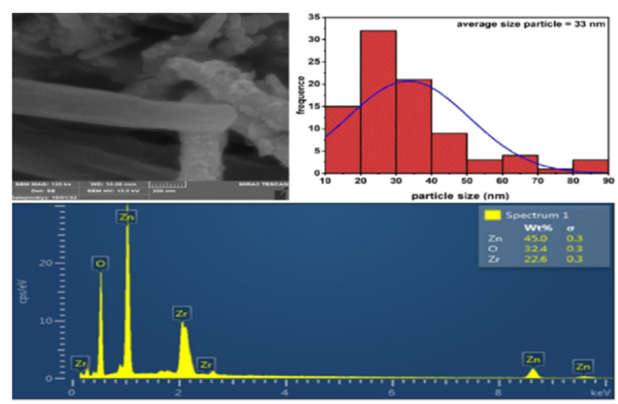

Fig. 8. Characterization of the surface shape of the G- ZnO: ZrO_2 nanocomposite and composition.

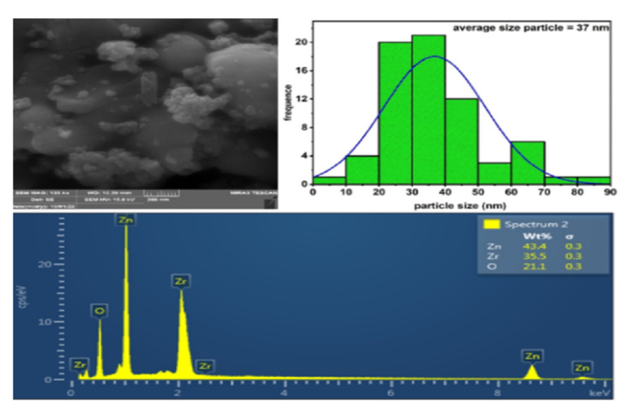

Fig. 9. Characterization of the surface shape of the S–ZnO: ZrO_2 nanocomposite and composition.

It is possible to determine the values of samples with negative surface charges for G-ZnO:ZrO_2 and S−ZnO:ZrO_2 nanocomposites as - 43 mV and - 26 mV, respectively, as shown in Figs. 10 and 11. Using the zeta potential analyzer, the surface charge of nanocomposites is evaluated. Their surface charge is a crucial attribute that impacts the structure, self-assembly, colloidal stability, and function of the nanocomposites [44]. Large positive or negative zeta potentials may explain the electrostatic repulsion between particles, which may have excellent physical colloidal stability. On the other hand, smaller zeta potentials affect the particles and may cause aggregations due to van der Waals forces [45]. This can be seen from the value of S−ZnO: ZrO_2 and comparing it to Fig. 10, where one can notice the presence of aggregation, unlike (G-ZnO: ZrO_2). In Fig. 10, it can be seen that the aggregation decreases due to its increasing values of - 43 mV, which improves stability.

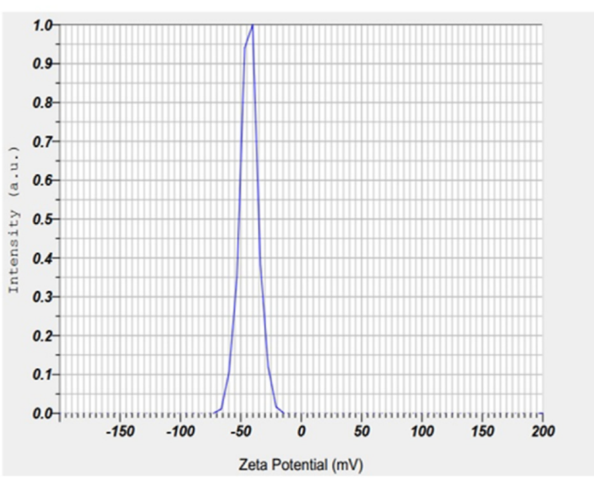

Fig. 10. Zeta potential analysis of G-ZnO:ZrO2 nanocomposite.

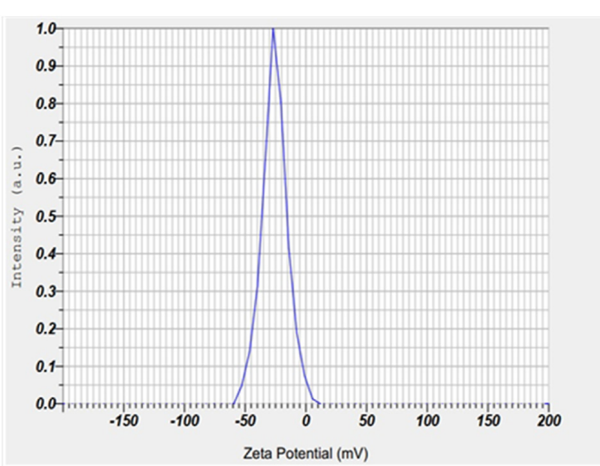

Fig. 11. Zeta potential analysis of S−ZnO:ZrO2 nanocomposite.

4. Antimicrobial activity

The effect of ZnO: ZrO_2 nanocomposite on different microbes was studied. Experimental results of G-ZnO: ZrO_2 and S−ZnO: ZrO_2 nanocomposites showed practical effects on (*S. aureus*, *E. coli*, *B. subtilis*, and *C. albicans*) were revealed in Fig. 12, which depicted the statistical analysis of bioactivity of (ZnO:ZrO_2) nanocomposites. The samples that were made kill different kinds of microbes. This is due to its small size; the G- ZrO: ZrO_2 nanocomposite can be anywhere from 10 to 90 nm in size, with 33 nm being the average. In contrast to the other sample, S− ZnO: ZrO_2, whose particle size ranges from (5−90), its average particle size is 37 nm, which contains agglomerates. It is possible to observe small-sized nanoparticles that easily penetrate the membrane. This penetration leads to cell death due to the leakage of the cell membrane [46]. The aggregation of nanoparticles has an effective role in influencing the activity of microbes because aggregation will increase the total volume and reduce the dispersion of nanoparticles in aqueous media. This leads to difficulty in interacting with nanocomposite and microbes and will reduce the overall antimicrobial potential [47]. Surface charge plays a major role in the process of landing microbes. The G-ZnO: ZrO_2 nanocomposite has a zeta potential of −43 mV. The agglomerations will decrease due to the repulsion of the particles as they carry high negative charges. In contrast to the S−ZnO nanocomposite, ZrO_2 has a zeta potential of −26 mV, and the agglomerations will increase. This is another reason, meaning that increasing the agglomerations has a role with the particle size in inhibiting or killing cells microbes, as mentioned in the literature [46,47]. The electrostatic interaction between nanocomposites and the surface of microbes is one aspect of inhibiting or killing microbial cells. An increase in a zeta potential surface charge also has a role in inhibiting or killing cells [48,49]. Oxide nanocomposites containing a band gap will generate hydroxyl radical (OH), hydrogen peroxide (H_2O_2) and superoxide ($O_2^{\bullet-}$), known as reactive oxygen species ROS [50,51]. These radicals can react with biological molecules (DNA, proteins, and lipids) leading to oxidative damage and apoptosis [52]. These data have a significant role in reducing the decrease in the S− ZnO: ZrO_2 sample. These particles in the two samples, with their small size and variety of shapes, as well as the presence of zinc ions, zirconium ions, high surface area, and high zeta value in one of the samples, help them easily penetrate the cell membrane, thus disrupting metabolism and other functions [53−56].

5. Anticancer activity of $ZnO:ZrO_2$ nanocomposite

Compared to compounds and nanoparticles made using physical and chemical methods, those made by the green synthesis method stand out for having a high degree of stability and being less toxic to living cells. This is due to the compounds and receptors in the plants used, which are responsible for reducing, covering, and stabilizing the effectiveness [42]. However, no study has been conducted on green composite ZnO: ZrO_2 with the same plants used in the present study on colon cancer and cell lines (HCT-116 and LoVo). Therefore, composite ZnO: ZrO_2 at concentrations of samples (1000, 500, 250, 125, and 62.5) μg/ml for (72 h) was determined through the MTT assay. After a series of complex processes and Using ELISA, absorbance is

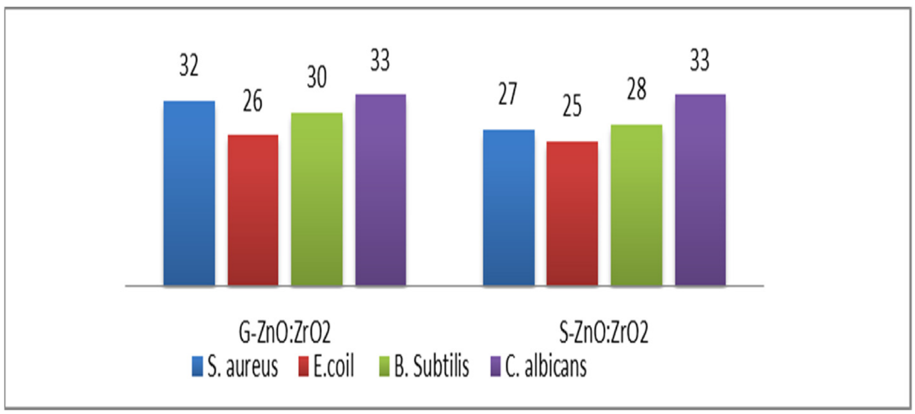

Fig. 12. Biological efficiency against microbes for G-ZnO:ZrO$_2$ and S–ZnO:ZrO$_2$ nanocomposite.

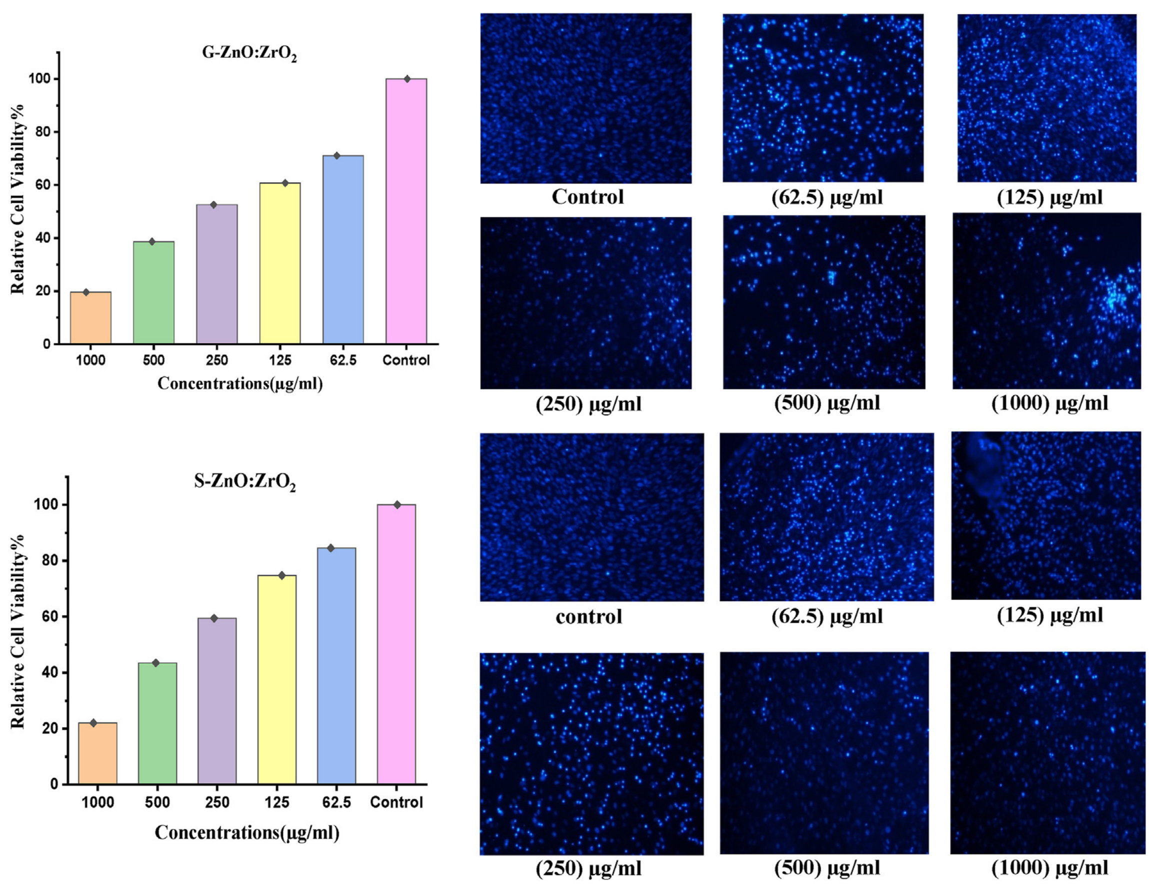

Fig. 13. The statistical representation and photographs of the killing stage in cancer cells of the HCT-116 cell line at different concentrations of G-ZnO:ZrO$_2$ and S–ZnO:ZrO$_2$ samples.

measured at 570 nm. Then, one could observe the dose dependent attenuation of the colon cancer cells by taking the captured optical images, as shown in Figs. 13 and 14, and Table 2. The morphological changes, such as cell shrinkage, rounding, and loss of stability, were apparent from the pictures. With increasing concentrations of ZnO: ZrO_2 as can be seen from Figs. 13 and 14, cell growth rates decrease with increasing sample concentration [57,58]. Since the particles are small size, the surface area of the substance will increase, which helps it to interact more. The increasing surface charge of the nanocomposite also plays a role. It is all directly proportional to the concentration of the nanocomposite. The mechanism of anticancer activity of green ZnO:ZrO_2 nanocomposite is related to the formation of reactive oxygen species (ROS), zinc ions and ZrO_2. ROS cause oxidative stress, which breaks down and destroys cell membranes and leads to apoptosis. ROS can also alter cell homeostasis, mitochondrial respiration, and redox damage [55].

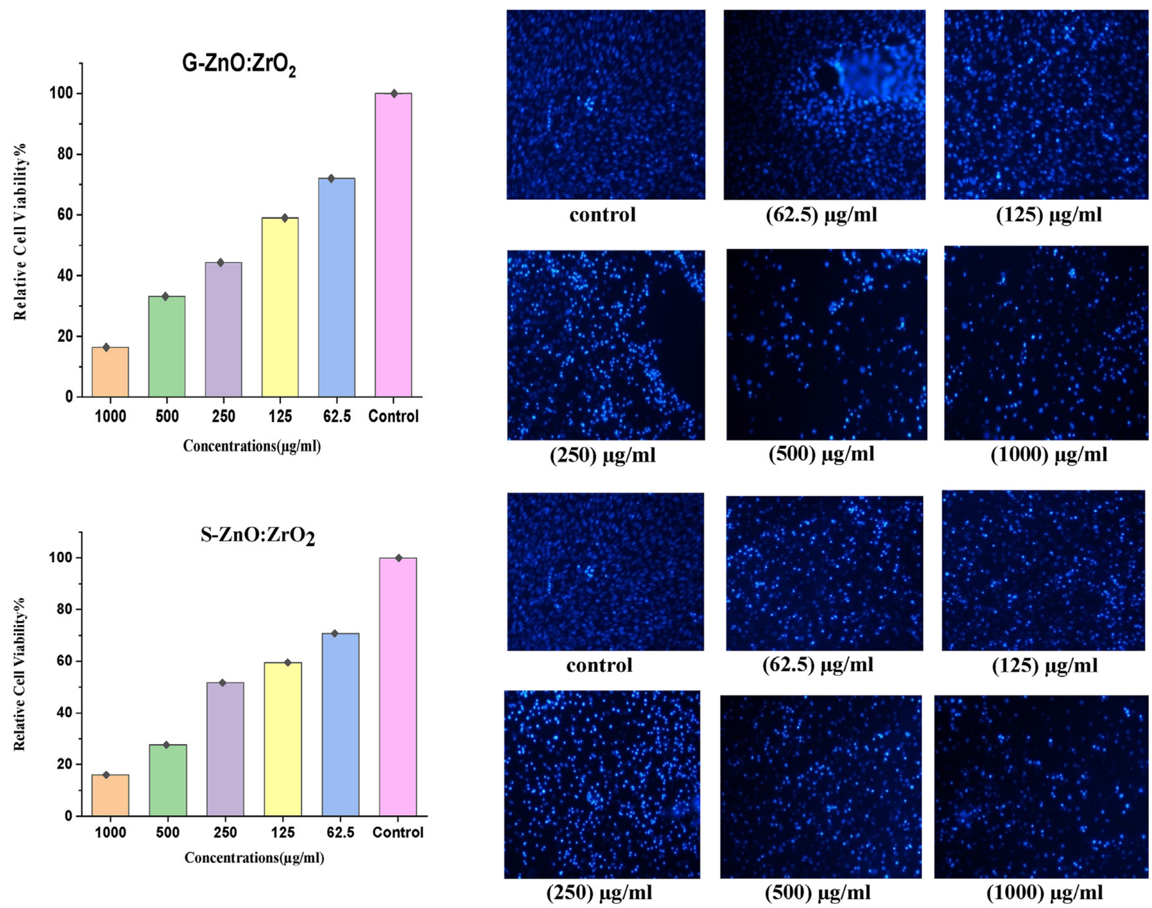

Fig. 14. The statistical representation and photographs of the killing stage in cancer cells of the LoVo cell line at different concentrations of G-ZnO:ZrO_2 and S–ZnO:ZrO_2 samples.

Table 2. The sample concentration (G-ZnO:ZrO_2 and S -ZnO:ZrO_2) and cell viability rate for each cell line (HCT-116 and LoVo).

Concentration (μg/ml)	Cell line (HCT-116)		Cell line (Lovo)	
	G-ZnO:ZrO_2	S–ZnO:ZrO_2	G-ZnO:ZrO_2	S–ZnO:ZrO_2
	Cell viability (%)	Cell viability (%)	Cell viability (%)	Cell viability (%)
1000	19.61904762	22.03174603	16.39902676	16.00973236
500	38.66666667	43.49206349	33.13868613	27.63990268
250	52.57142857	59.42857143	44.33090024	51.63017032
125	60.76190476	74.73015873	58.97810219	59.513382
62.5	71.04761905	84.50793651	72.01946472	70.75425791
0	100	100	100	100

6. Conclusions

The study investigated how to characterize G-ZnO:ZrO_2 (*Z. officinale*) and S−ZnO:ZrO_2 (*S. aromaticum*) using the green method with two plant extracts. The structure of G-ZnO: ZrO_2 was a hexagonal phase of ZnO, while ZrO_2 is a monoclinic and a tetragonal phase, and S−ZnO: ZrO_2 is a hexagonal phase of ZnO, while ZrO_2 is a tetragonal phase. For the composite G-ZnO: ZrO_2 and S−ZnO: ZrO_2 NPs, the average crystallite sizes were 24.48 nm and 21.84 nm, respectively. Spherical nanoparticles were randomly spread over needle-like particles in the G-ZnO: ZrO_2 and spherical, lobed nanoparticles with mostly smooth agglomerates in the S−ZnO: ZrO_2 that were made. Fourier transformed infrared of prepared samples revealed significant absorption peaks for organic and inorganic. The prepared samples had direct energy gaps and overlapping gap levels between the oxide gaps. The zeta potential for G-ZnO: ZrO_2 had a more significant value (−43 mV) than that for S−ZnO: ZrO_2 (−26 mV). The outcome of this investigation confirms the potential of prepared, environmentally friendly samples with active agents for anticancer activity and antimicrobial activity applications. There was an effect on both samples, and precise positive results were observed, especially in the G-ZnO: ZrO_2 sample.

Ethical information

The research undertaken in the submitted articles adhered to ethical and responsible practices. This study did not include any human or animal subjects.

Conflict of interest

The authors declare that they have no competing interests in this.

Funding

There is no funding for this research.

Acknowledgment

The authors are deeply indebted to the administration of the Department of Physics, College of Science, University of Baghdad, Iraq, and the Directorate of Agricultural Research of the Ministry of Science and Technology in Iraq for their help to this work.

References

[1] M. Yadi, M. Mostafavi, B. Saleh, S. Davaran, I. Aliyeva, R. Khalilov, M. Nikzamir, N. Nikzamir, A. Akbarzadeh, Y. Panahi, M. Milani, Current developments in green synthesis of metallic nanoparticles using plant extracts: a review, artificial cells, Nanomed Biotechnol 46 (2018) 336−343, https://doi.org/10.1080/21691401.2018.1492931.
[2] K. Pal, S. Chakrobrty, N. Nath, Limitations of nanomaterials insights in green chemistry sustainable route: review on novel applications, Green Process Synth 11 (2022) 951−964, https://doi.org/10.1515/gps-2022-0081.
[3] S. Ahmed, M. Ahmad, B.L. Swami, S. Ikram, A review on plants extract mediated synthesis of silver nanoparticles for antimicrobial applications: a green expertise, J Adv Res 7 (2016) 17−28, https://doi.org/10.1016/j.jare.2015.02.007.
[4] S. Fakhari, M. Jamzad, H.K. Fard, Green synthesis of zinc oxide nanoparticles: a comparison, Green Chem Lett Rev 12 (2019) 19−24, https://doi.org/10.1080/17518253.2018.1547925. .
[5] J. H. Patil Liny, Nanocomposites − an overview of classification and applications, J Emerg Technol Innov Res 8 (2021) 681−690.
[6] M. Sen, Nanocomposite Materials. Nanotechnology and the Environment, Amity University, Noida, Uttar Pradesh, India. 2020, pp. 107−118. https://dio.org/10.5772/intechopen.93047.
[7] P.H.C. Camargo, K.G. Satyanarayana, F. Wypych, Nanocomposites: synthesis, structure, properties and new application opportunities, Mater Res 12 (2019) 1−39, https://doi.org/10.1590/S1516-14392009000100002.
[8] B. Sathyaseelan, E. Manikandan, I. Baskaran, K. Senthilnathan, K. Sivakumar, M.K. Moodley, R. Ladchumananandasivam, M. Maaza, Studies on structural and optical properties of ZrO2 nanopowder foropto-electronic applications, J Alloys Compd 694 (2017) 556−559, https://doi.org/10.1016/j.jallcom.2016.10.002.
[9] A.S. Keiteb, E. Saion, A. Zakaria, N. Soltani, Structural and optical properties of zirconia nanoparticles by thermal treatment synthesis, J Nanomater 2016 (2016) 1−6, https://doi.org/10.1155/2016/1913609.
[10] A.M. Bannunah, Biomedical applications of zirconia-based nanomaterials: challenges and future perspectives, Molecules 28 (2023) 1−17, https://doi.org/10.3390/molecules28145428.
[11] F. Qunbo, W. Fuchi, Z. Huiling, Z. Feng, Study of ZrO2 phase structure and electronic properties, Mol Simulat 34 (2008) 1099−1103, https://doi.org/10.1080/08927020802101759.
[12] T.F. Saeid, A. Ramazani, S. Moradi, P.A. Asiabi, Green synthesis of zinc oxide nanoparticles using Arabic gum and photocatalytic degradation of direct blue 129 dye under visible light, J Mater Sci Mater Electron 28 (2017) 13596−13601, https://doi.org/10.1007/s10854-017-7199-5.
[13] H. Morkoç, Ü. Özgür, Zinc Oxide: Fundamentals, Materials and Device Technology, John Wiley & Sons. 2008, https://doi.org/10.1002/9783527623945.
[14] C. Jagadish, S. Pearton, Zinc Oxide Bulk, Thin Films and Nanostructures: Processing, Properties, and Applications, Elsevier. 2011.
[15] S. Haq, H. Afsar, M.B. Ali, M. Almalki, B. Albogami, A. Hedfi, Green synthesis and characterization of a ZnO-ZrO2 heterojunction for environmental and biological applications, Crystals 11 (2021) 1−12, https://doi.org/10.3390/cryst11121502.
[16] M. Ali, M. Ikram, M. Ijaz, A. Ul-Hamid, M. Avais, A.A. Anjum, Green synthesis and evaluation of n-type ZnO nanoparticles doped with plant extract as alternative antibacterials, Appl Nanosci 10 (2020) 3787−3803, https://doi.org/10.1007/s13204-020-01451-6.
[17] S.M. Abed, Y.S. Mahmood, I.F. Waheed, A.M. Alwan, Antibacterial activity of green synthesized copper oxide nanoparticles, Iraqi J Sci 62 (2021) 3372−3383, https://doi.org/10.24996/ijs.2021.62.9(S.I.).8.
[18] G. Busch, H. Schade, Lectures on Solid State Physics, Pergamon Press. 2013.
[19] M.J. Tuama, M.F.A. Alias, Synthesis and characterization of zirconium oxide nanoparticles using Z. officinale and S. aromaticum plant extracts for antibacterial application, Karbala Int J Modern Sci 9 (2023) 698−711, https://doi.org/10.33640/2405-609X.3331.

[20] Sh Aghabeygi, M. Zare-Dehnavi, Sono synthesis and characterization of ZrO2/ZnO nanocomposite, composition effect on enhancing photocatalytic properties, Int J Nano Dimens (IJND) 6 (2015) 297−304, sid.ir/paper/322236.

[21] I. Danilenko, O. Gorban, S. Gorban, G. Volkova, V. Glazunova, T. Konstantinova, Production of composite ZrO2-ZnO nanoparticles using advanced co-precipitation process and determination their photo-oxidative properties by oxidation of C60 fullerene, in: IEEE 8th International Conference on Nanomaterials: Applications & Properties, 2018, pp. 1−5, https://doi.org/10.1109/NAP.2018.8914836.

[22] M.L. Hossain, L.Y. Lim, K. Hammer, D. Hettiarachchi, C. Locher, A Review of commonly used methodologies for assessing the antibacterial activity of honey and honey products, Antibiotics 11 (2022) 1−17, https://doi.org/10.3390/antibiotics11070975.

[23] E. Chung, G. Ren, I. Johnston, R.K. Matharu, L. Ciric, A. Walecka, Y.K. Cheong, Applied methods to assess the antimicrobial activity of aetallic-based nanoparticles, Bioengineering 10 (2013) 1−17, https://doi.org/10.3390/bioengineering10111259.

[24] S.S. Salem, A.H. Hashem, A.L.M. Sallam, A.S. Doghish, A.A. Al-Askar, A.A. Arishi, A.M. Shehabeldine, Synthesis of silver nanocomposite based on carboxymethyl cellulose: antibacterial, antifungal and anticancer Activities, Polymers 14 (2022) 1−16, https://doi.org/10.3390/polym14163352.

[25] W.S. Dong, F.Q. Lin, C.L. Liu, M.Y. Li, Synthesis of ZrO2 nanowires by ionic-liquid route, J Colloid Interface Sci 333 (2009) 734−740, https://doi.org/10.1016/j.jcis.2009.02.025.

[26] R. Bekkari, L. Laânab, B. Jaber, Effect of the bivalent dopant ionic radius, electronegativity and concentration on the physical properties of the sol−gel-derived ZnO thin films, J Mater Sci Mater Electron 31 (2020) 15129−15139, https://doi.org/10.1007/s10854-020-04078-z.

[27] R.A. Rasheed, M.F.A. Alias, The role of aluminum doping on structural and optical properties of ZnO thin films prepared by PLD, I.O.P. Conf. Ser, Mater Sci Eng 757 (2020) 1−11, https://doi.org/10.1088/1757899X/757/1/012056.

[28] A.H. Alkhathlan, H.A. Al-Abdulkarim, M. Khan, M. Khan, M. Alkholief, A. Alshamsan, A. Almomen, N. Albekairi, H.Z. Alkhathlan, M.R.H. Siddiqui, Evaluation of the anticancer activity of phytomolecules conjugated gold nanoparticles synthesized by aqueous extracts of zingiber officinale (ginger) and nigella sativa L. seeds (black cumin), Materials 14 (2021) 1−17, https://doi.org/10.3390/ma14123368.

[29] B. Abdullah, D. Heryanto, Makassar Tahir, Quantitative analysis of X-Ray diffraction spectra for determine structural properties and deformation energy of Al, Cu and Si, J Phys Conf 1317 (2019) 1−11. https://doi:10.1088/1742-6596/1317/1/012052.

[30] H. Purnomo, F. Jaya, S.B. Widjanarko, The effects of type and time of thermal processing on ginger (zingiber officinale roscoe) rhizome antioxidant compounds and its quality, Int Food Res J 17 (2010) 335−347.

[31] I.K. Amponsah, A. Boakye, E. Orman, F.A. Armah, L.S. Borquaye, S. Adjei, Y.A. Dwamena, K.A. Baah, B.K. Harley, Assessment of some quality parameters and chemometric-assisted FTIR spectral analysis of commercial powdered ginger products on the Ghanaian market, Heliyon 8 (2022) e09150, https://doi.org/10.1016/j.heliyon.2022.e09150, 1-9.

[32] A.B.D. Nandiyanto, R. Oktiani, R. Ragadhita, How to read and interpret FTIR spectroscope of organic material, Indonesia, J Sci Technol 4 (2019) 97−118, https://doi.org/10.17509/ijost.v4i1.15806.

[33] A. Kr Archana, R Kr Aman, N. Kr Singh, A. Jabeen, Effect of superfine grinding on structural, morphological and antioxidant properties of ginger (zingiber officinale) nanocrystalline food powder, Mater Today Proc 43 (2021) 3397−3403, https://doi.org/10.1016/j.matpr.2020.09.028.

[34] K.S. Khashan, G.M. Sulaiman, S.A. Hussain, Synthesis and characterization of aluminum doped zinc oxide nanostructures by Nd:YAG laser in liquid, Iraqi J Sci 61 (2020) 2590−2598, https://doi.org/10.24996/ijs.2020.61.10.15.

[35] N. Muthulakshmi, A. Kathirvel, R. Subramanian, M. Senthil, Biofabrication of zirconia nanoparticles: synthesis, spectral characterization and biological activity evaluation against pathogenic bacteria, Biointerf Res Appl Chem 13 (2023) 1−12, https://doi.org/10.33263/BRIAC123.190.

[36] P. Parthipan, M.S. AlSalhi, S. Devanesan, A. Rajasekar, Evaluation of syzygium aromaticum aqueous extract as an eco-friendly inhibitor for microbiologically influenced corrosion of carbon steel in oil reservoir environment, Bioproc Biosyst Eng 44 (2021) 1441−1452, https://doi.org/10.1007/s00449-021-02524-8.

[37] S. Yedurkar, C. Maurya, P. Mahanwar, Biosynthesis of zinc oxide nanoparticles using ixora coccinea leaf extract-a green approach, Open J Synth Theor Appl 5 (2016) 1−14, https://doi.org/10.4236/ojsta.2016.51001.

[38] M. Anvarinezhad, A. Javadi, H. Jafarizadeh-Malmiri, Green approach in fabrication of photocatalytic, antimicrobial, and antioxidant zinc oxide nanoparticles - hydrothermal synthesis using clove hydroalcoholic extract and optimization of the process, Green Process Synth 9 (2020) 375−385, https://doi.org/10.1515/gps-2020-0040.

[39] A.H. Kianfar, M.A. Arayesh, M.M. Momeni, Degradation of M.B. and RhB by modified ZrO2 nanoparticles via sunlight, Appl Phys Mater Sci Process 27 (2021) 1−9, https://doi.org/10.1007/s00339-020-04257-z.

[40] M. Aminuzzaman, L.P. Ying, W. Goh, A. Watanabe, Green synthesis of zinc oxide nanoparticles using aqueous extract of garcinia mangostana fruit pericarp and their photocatalytic activity, Bull Mater Sci 41 (2018) 1−10, https://doi.org/10.1007/s12034-018-1568-4.

[41] J.E.M. Mastache, O.S. Vargas, R. López, F.M. Morales, K.M. A. Gomez, A.B. Lara, A. Coyopol, J.N. Jiménez, E.G. Alcántara, N.C. Castro, G. Escalante, Study of the properties of zirconia nanoparticles/zinc oxide films composites: comparation to thermally treated samples, Result Chem 6 (2023) 1−10, https://doi.org/10.1016/j.rechem.2023.101230.

[42] H. Agarwal, A. Nakara, S. Menon, V.K. Shanmugam, Eco-friendly synthesis of zinc oxide nanoparticles using cinnamomum tamala leaf extract and its promising effect towards the antibacterial activity, J Drug Deliv Sci Technol 53 (2019) 1−23, https://doi.org/10.1016/j.jddst.2019.101212.

[43] I.-M. Chung, A.A. Rahuman, S. Marimuthu, A.V. Kirthi, K. Anbarasan, G. Rajakumar, An investigation of the cytotoxicity and caspase-mediated apoptotic effect of green synthesized zinc oxide nanoparticles using eclipta prostrata on human liver carcinoma cells, Nanomaterials 5 (2015) 1317−1330, https://doi.org/10.3390/nano5031317.

[44] S.G. Khalil, M.M. Mutter, Z.K. Mohammed, G. Salem, Fabrication and characterization of a gas sensor from ZrO2: MgO nanostructure thin films by R.F. magnetron sputtering technique, Baghdad Sci J 16 (2019) 199−208, https://doi.org/10.21123/bsj.2019.16.1(Suppl.).0199.

[45] Z. Abbas, C. Labbez, S. Nordholm, E. Ahlberg, Size-dependent surface charging of nanoparticles, J Phys Chem C112 (2008) 5715−5723, https://doi.org/10.1021/jp709667u.

[46] S. Bhattacharjee, Review article D.L.S. and zeta potential − what they are and are not, J Contr Release 235 (2016) 337−351, https://doi.org/10.1016/j.jconrel.2016.06.017.

[47] M. Vielkind, I. Kampen, A. Kwade, Zinc oxide nanoparticles in bacterial growth medium: optimized dispersion and growth inhibition of pseudomonas putida, Adv Nanoparticles 2 (2013) 287−293, https://doi.org/10.4236/anp.2013.24039.

[48] K.R. Raghupathi, R.T. Koodali, A.C. Manna, Size-dependent bacterial growth inhibition and mechanism of antibacterial activity of zinc oxide nanoparticles, Langmuir 27 (2011) 4020−4028, https://doi.org/10.1021/la104825u.

[49] M.S. Wong, C.W. Chun, C.C. Hsieh, S.C. Hung, D.S. Sun, H. H. Chang, Antibacterial property of Ag nanoparticle-impregnated N-doped titania films under visible light, Sci Rep 5 (2015) 1−11, https://doi.org/10.1038/srep11978.

[50] S. Shamaila, N. Zafar, S. Riaz, R. Sharif, J. Nazir, S. Naseem, Gold nanoparticles: an efficient antimicrobial agent against

enteric bacterial human pathogen, Nanomaterials 6 (2016) 1−10, https://doi.org/10.3390/nano6040071.
[51] N. Padmavathy, R. Vijayaraghavan, Enhanced bioactivity of ZnO nanoparticles- an antimicrobial study, Sci Technol Adv Mater 9 (2008) 1−7. https://doi:10.1088/1468-6996/9/3/035004.
[52] T. Gordon, B. Perlstein, O. Houbara, I. Felner, E. Banin, S. Margel, Synthesis and characterization of zinc/iron oxide composite nanoparticles and their antibacterial properties, Colloids Surf A Physicochem Eng Asp 374 (2011) 1−8. https://doi:10.1016/j.colsurfa.2010.10.015.
[53] V. Sharma, D. Anderson, A. Dhawan, Zinc oxide nanoparticles induce oxidative DNA damage and ROS-triggered mitochondria mediated apoptosis in human liver cells (HepG2), Apoptosis 17 (2012) 852−870. https://doi:10.1007/s10495-012-0705-6.
[54] M. Kumaresan, K. Vijai Anand, K. Govindaraju, S. Tamilselvan, V. Ganesh Kumar, Seaweed sargassum wightii mediated preparation of zirconia (ZrO2) nanoparticles and their antibacterial activity against gram-positive and gram-negative bacteria, Microb Pathog 124 (2018) 311−315, https://doi.org/10.1016/j.micpath.2018.08.060.
[55] M.F.A. Alias, A.S. Abd-Alsada, The influence of zinc oxide with carbon nanotube composite nanomaterials on antibacterial activity, J Phys Conf Ser 2114 (2021) 1−9, https://doi.org/10.1088/17426596/2114/1/012089.
[56] H. Agarwal, S. Menon, S.V. Kumar, S. Rajeshkumar, Mechanistic study on antibacterial action of zinc oxide nanoparticles synthesized using green route, Chem Biol Interact 286 (2018) 60−70, https://doi.org/10.1016/j.cbi.2018.03.008.
[57] K. Karthik, M. Shashank, V. Revathi, T. Tatarchuk, Facile microwave-assisted green synthesis of NiO nanoparticles from andrographis paniculata leaf extract and evaluation of their photocatalytic and anticancer activities, Mol Cryst Liq Cryst 673 (2018) 70−80, https://doi.org/10.1080/15421406.2019.1578495.
[58] E. Sarala, M. Madhukara Naik, M. Vinuth, Y.V. Rami Reddy, H.R. Sujatha, Green synthesis of lawsonia inermis-mediated zinc ferrite nanoparticles for magnetic studies and anticancer activity against breast cancer (MCF-7) cell lines, J Mater Sci Mater Electron 31 (2020) 8589−8596, https://doi.org/10.1007/s10854-020-03394-8.